Advanced Numerical Modeling and Experimental Analysis of Thermal Gradients in Gleeble Compression Configuration for 2017-T4 Aluminum Alloy

Olivier Pantalé, Yannis Muller, Yannick Balcaen

applied mechanics

MDPI

Article

Advanced Numerical Modeling and Experimental Analysis of Thermal Gradients in Gleeble Compression Configuration for 2017-T4 Aluminum Alloy

Olivier Pantalé *, Yannis Muller and Yannick Balcaen

Laboratoire Génie de Production, Université de Technologie de Tarbes Occitanie Pyrénées, Université de Toulouse, 47 Av d'Azereix, 65016 Tarbes, France; yannis.muller@etudiant.uttop.fr (Y.M.); yannick.balcaen@uttop.fr (Y.B.)
* Correspondence: olivier.pantale@uttop.fr; Tel.: +33-562-442-933

Abstract: Gleeble thermomechanical simulators are widely utilized tools for the investigation of high-temperature deformation behavior in materials. However, temperature gradients that develop within the specimen during Gleeble compression tests have the potential to result in non-uniform deformation, which may subsequently impact the accuracy of the measured mechanical properties. This study presents an experimental and numerical investigation of the temperature fields in 2017-T4 aluminum alloy specimens prior to Gleeble compression tests at temperatures ranging from 300 °C to 500 °C utilizing uniform temperature distribution (ISO-T) tungsten carbide anvils. The use of multiple thermocouples, welded to both the specimen and anvils, offers valuable insights into the temperature gradients and their evolutions. A coupled thermal–electrical finite-element model was developed in Abaqus for the purpose of simulating the resistive heating process. A user amplitude subroutine (UAMP) is implemented to regulate the heating based on a proportional–integral–derivative (PID) algorithm that modulates the current density to follow the specified temperature profile. The numerical results demonstrate that the temperature gradients within the specimen at the end of the heating process, reaching a temperature of 400 °C, are minimal, with values below 1.9 °C. This is in accordance with the experimental observations. The addition of graphite foils between the specimen and anvils has been shown to effectively reduce the gradients. The use of the measured anvil temperature as a boundary condition, rather than a constant value of 20 °C, has been demonstrated to improve the agreement between the simulated and experimental cooling curves. The modeling approach provides a framework for quantifying temperature gradients in Gleeble compression specimens and for assessing their impact on the measured constitutive response of materials at elevated temperatures.

Keywords: Gleeble compression test; 2017-T4 aluminum alloy; thermal gradient; numerical simulation; abaqus; coupled electro-thermal model; user amplitude subroutine

Citation: Pantalé, O.; Muller, Y.; Balcaen, Y. Advanced Numerical Modeling and Experimental Analysis of Thermal Gradients in Gleeble Compression Configuration for 2017-T4 Aluminum Alloy. *Appl. Mech.* **2024**, *5*, 839–855. https://doi.org/10.3390/applmech5040047

Received: 30 September 2024
Revised: 29 October 2024
Accepted: 6 November 2024
Published: 13 November 2024

1. Introduction

Gleeble thermomechanical simulation systems are common tools for studying the high-temperature deformation behavior of materials through tensile [1] or compression tests [2]. These systems permit the precise control of temperature profiles and deformation conditions, thereby enabling the replication of the thermal and mechanical processing that materials undergo during manufacturing operations such as forging, rolling, and welding. However, a well-documented challenge in Gleeble iso-thermal compression testing is the presence of temperature gradients within the specimen, which can lead to non-uniform deformation and affect the accuracy of the reported mechanical properties, as highlighted by Gao et al. [3] or Quan et al. [4]. The development of temperature gradients within specimens during Gleeble compression tests is attributable to a number of factors. Heat transfer occurs from the specimen to the anvil assembly and their cooled grips.

Furthermore, the development of thermal gradients within the specimen itself, coupled with the generation of heat from plastic deformation, contribute to this phenomenon. Jedrasiak et al. [5] demonstrated that, for a titanium alloy, the temperature is highest at the center of the specimen and decreases towards the anvils, with the steepest gradients observed near the anvil contact interfaces. The non-uniform deformation resulting from temperature gradients in Gleeble compression specimens can cause the measured flow stress and mechanical properties to deviate from the true bulk material behavior. This introduces inaccuracies in process modeling and material characterization, as well as the need for flow stress correction procedures, as proposed by Xiao et al. [6].

A substantial amount of research has been conducted to examine the influence of temperature gradients on the deformation behavior and microstructural evolution during Gleeble compression tests [4,7,8]. Finite element (FE) modeling has emerged as a powerful tool for analyzing the temperature distributions and resulting strain fields within the specimen during these tests. Coupling the FE simulations with experimental measurements, as proposed by Yu et al. [9], represents a promising avenue for advancing our understanding of the effects of temperature gradients on deformation behavior. Researchers may also employ experimental techniques such as digital image correlation (DIC), as proposed by Coelho et al. [10], to gain insights into the influence of temperature gradients on deformation behavior and to develop correction methodologies. The impact of temperature gradients on microstructure evolution analysis has been the subject of investigation by numerous researchers. Quan et al. [4] developed a coupled thermo-electric–mechanical model to account for these effects, emphasizing the substantial influence of temperature gradients on the experimental outcomes. Similarly, Xiao et al. [6] proposed a coupled thermo-electric–mechanical finite element (FE) model for the hot compression testing of TA15 titanium alloy. The model simulates the intricate interactions between temperature, electrical current, and deformation within the specimen. The predictions from the finite element (FE) model are then employed in an inverse analysis procedure, wherein the input flow stress is iteratively adjusted until the predicted deformation response aligns with the experimentally observed response. This methodology yields a corrected flow stress that more accurately reflects the intrinsic material behavior, accounting for the influence of temperature gradients and other coupled effects. Zhang et al. [1] highlighted the significant influence of the thermal gradient on the mechanical properties of metallic materials during Gleeble compression tests, noting its impact on flow stress, microstructural evolution, and overall material behavior. Furthermore, they underscored the necessity of comprehending these effects for precise material characterization and processing. Recent studies on various alloys have demonstrated that temperature and strain exert a significant influence on the degree of dynamic recrystallization (DRX) during compression testing. Among numerous studies, Cheng et al. [11] investigated the behavior of magnesium alloys and found that the extent of DRX varies with both temperature and strain, indicating that thermal gradients can substantially alter the microstructural evolution during compression. Similarly, Tize Mha et al. [12] studied medium carbon steels and observed that the DRX mechanisms change depending on the temperature, with continuous and discontinuous DRX occurring at different thermal conditions. While the thermal gradient can sometimes help modify local flow stresses through controlled microstructural changes in full-scale forgings, it also poses challenges in accurately measuring and interpreting these properties at the testing specimen scale.

The objective of the present study is to develop an advanced numerical model for simulating the electro-thermal behavior of a 2017-T4 aluminum alloy prior to Gleeble isothermal compression tests and to validate it against detailed experimental measurements. This study has two principal objectives. Initially, Gleeble heating tests will be conducted at temperatures ranging from 300 °C to 500 °C, with the use of multiple thermocouples to measure the temperature evolution and gradients within the specimen and anvils. Secondly, a coupled thermal–electrical finite element model will be developed in Abaqus [13] to simulate the resistive heating process, including the specimen, ISO-T tungsten carbide

anvils, and graphite foils at the interfaces. The temperature field inside the specimen will be determined at the conclusion of the heating phase. This will account for the non-homogeneity of the temperature field and its influence on the compression behavior, thereby enabling a more accurate characterization of the material's response under realistic thermal conditions. Accordingly, the study aims to integrate a user amplitude subroutine (UAMP) to regulate the heating process by calculating the requisite current density to adhere to the specified temperature profile, emulating Gleeble's proportional–integral–derivative (PID) control system. The numerical outcomes will be evaluated in comparison with the experimental data in terms of the temperature evolution at pivotal locations and the heating power. Ultimately, the necessity of accurately capturing the actual anvil cooling conditions in the simulations will be evaluated.

In this paper, we address some gaps in the understanding and modeling of thermal gradients during Gleeble compression tests, particularly for aluminum alloys. As introduced earlier, previous research has highlighted the challenges posed by temperature gradients in these tests, which can lead to non-uniform deformation and inaccuracies in mechanical property measurements. The proposed model advances this field by developing a coupled thermal–electrical finite element model that accurately simulates the resistance heating process, incorporating real-time temperature feedback through a UAMP to emulate Gleeble's PID control system. By integrating experimental data from multiple thermocouples and using graphite foils to reduce thermal gradients, our approach not only improves the accuracy of temperature control, but also increases the reliability of the measured mechanical properties. This study provides a robust framework for quantifying and mitigating the effects of temperature gradients in Gleeble tests, thereby enabling more accurate material characterization under realistic thermal conditions.

The present paper's Section 2 describes the experimental setup, including the Gleeble system configuration, specimen and anvil geometries, thermocouple locations, and test procedures. The results of the representative test conducted at 400 °C are presented in detail. Section 3 details the development of the axisymmetric electro-thermal finite element model in Abaqus, the material properties used, and the implementation of the UAMP subroutine for heating control. Section 4 compares the numerical results with the experimental measurements for two cases: a constant 20 °C heat sink at the anvil rear face and the use of the measured anvil temperature as the boundary condition. The temperature fields within the specimen and anvils are analyzed. Finally, Section 5 summarizes the main conclusions of the study and provides recommendations for future work.

2. Gleeble Thermomechanical Simulator

2.1. Experimental Setup

Compression tests were conducted using a Gleeble 3500 thermomechanical simulator, as illustrated in Figure 1. The specimen is a cylinder with a diameter of 10 mm. The specimen, measuring $d = 10$ mm in diameter and $L = 15$ mm in length, is composed of aluminum 2017-T4 and is held between two ISO-T Tungsten carbide (WC-Co) anvils. The ISO-T anvils are designed with the specific purpose of minimizing thermal gradients and mechanical inconsistencies during the compression process. As reported by Bennett et al. [14], the use of these anvils helps achieve isothermal conditions, which are critical for obtaining reliable flow stress data across a range of temperatures and strain rates.

Aluminum 2017-T4 was chosen for convenience, as this material is widely used in industry. The aim here is not to focus on a specific type of material, but to develop an electro-thermo-mechanical model capable of simulating the temperature gradients present in the sample. Similarly, the choice of temperature range for the study was based on the maximum operating temperature of the material and the need for a sufficiently representative range in terms of amplitude.

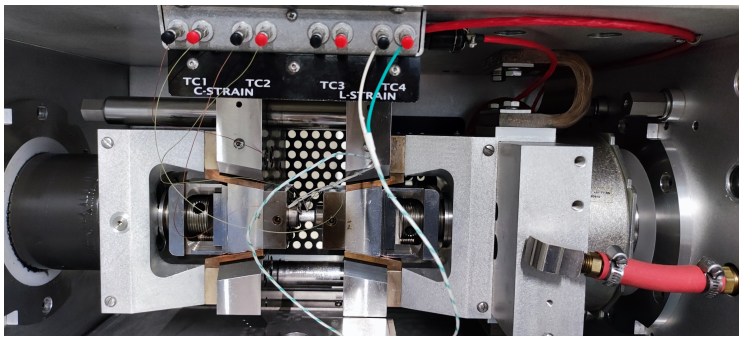

Figure 1. Closed view of the specimen inside the Gleeble thermomechanical simulator.

Figure 2 depicts a schematic block diagram of the internal configuration of the Gleeble apparatus utilized in the experimental procedures. The moving jaw, situated on the left side, imposes a displacement on the specimen, while the fixed jaw on the right side measures the axial load applied to the specimen via a force sensor. The force sensor has a specified capacity of 111 kN, thereby ensuring its ability to accommodate the anticipated load range during testing. The jaws are connected to a hydraulic servo system that is capable of applying compressive or tensile forces to deform the specimen. A water cooling system is located inside the jaws. In order to minimize the convective cooling of the sample and achieve a more uniform temperature distribution across the specimen, as reported by Bennett et al. [15], the tests are conducted under rough vacuum conditions (30–40 Pa). An L-gauge measures the relative displacement of the jaws.

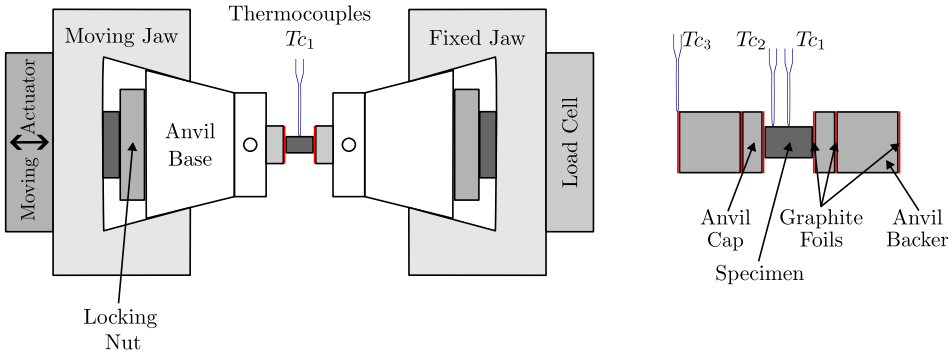

Figure 2. Gleeble compression test configuration: (**left**) global view and (**right**) closed view of the specimen and the anvils.

To guarantee optimal electrical and thermal contact between the specimen and the anvils without inducing premature deformation, a constant compression force of $F = 0.5$ kN is applied during the heating phase. This force is sufficiently small to avoid altering the specimen's behavior while remaining sufficient to maintain proper contact conditions. It is imperative that this force be maintained in order to ensure consistent contact, which is a prerequisite for accurate and reliable measurements. As illustrated in the right portion of Figure 2, the ISO-T anvils are composed of two principal components: the cap and the backer. The cap has a diameter of $^3/_4$ in (19.05 mm) and a length of $^1/_4$ in (6.35 mm), while the backer has a length and a diameter of $^3/_4$ in. The rear face of the anvil backer is in contact with a copper pad with a thickness of $^1/_{30}$ in (approx. 0.83 mm). The anvil base and the jaws' copper pads facilitate the cooling of the specimen through the Gleeble's internal cooling system, which circulates water at a regulated temperature of 20 °C $^{+1}/_{-2}$ °C.

A single graphite foil with a thickness of $^5/_{1000}$ in (0.127 mm) is positioned between the sample and the anvil. Two additional graphite foils with a thickness of $^{10}/_{1000}$ in (0.254 mm) are also included between the cap and the backer of the anvil, and two additional graphite foils with a thickness of $^5/_{1000}$ in are inserted between the anvil backer and the copper pad. The objective of utilizing these graphite foils is twofold: firstly, to diminish the frictional

resistance between the sample and the anvil during the compression phase, and secondly, to minimize the thermal gradient within the sample during the heating phase. Graphite foils are frequently employed in Gleeble thermomechanical simulation tests to mitigate friction at the specimen–anvil interface. This is due to their low friction coefficient, which typically ranges from approximately $\mu = 0.1$, as reported by Akerström et al. [16]. This coefficient enables more uniform deformation of the specimen during compression. One of the challenges encountered when implementing a numerical model for electro-thermo-mechanical behavior is the anisotropic nature of graphite foils' behavior, as reported by numerous authors [17–21]. A comprehensive review of the flexible graphite thermophysical properties is provided by Solfiti et al. [22]. As reported by Inagaki et al. [23], this anisotropy is primarily attributed to the strong covalent bonding within the layers and the weaker van der Waals forces between them. These characteristics facilitate electron and phonon transport along the planes but restrict it across the layers.

The thermal conductivity of graphite sheets has been shown to vary significantly depending on the orientation of the material, as reported by Inagaki et al. [23]. The thermal conductivity along the basal plane often reaches values between 700 W/mK and 1500 W/mK, which is significantly higher than that of metals like copper. However, the through-plane thermal conductivity of graphite foils is considerably lower, typically around 5 W/mK, which provides thermal insulation that helps to reduce temperature gradients within the specimen during resistive heating, as reported by Gao et al. [3].

Furthermore, the electrical properties of graphite exhibit pronounced anisotropy, rendering transverse measurements particularly challenging, as documented by Janerka et al. [24]. The delocalized π-electron system within the graphene layers facilitates high electrical conductivity along the plane, while the conductivity perpendicular to the layers is considerably lower due to the lack of effective charge carrier mobility in that direction, as reported by Sariyev et al. [25]. The high electrical resistivity of graphite, which is approximately $10^{-3}\ \Omega\,\mathrm{m}$ when measured perpendicular to the surface, as reported by Cermak et al. [20], contributes to the thermal insulation effect by limiting heat loss from the specimen to the anvils through a thermo-resistive mechanism. Gong et al. [26] states that this disparity concerning electrical and thermal properties is crucial in applications such as thermal management systems, where efficient heat dissipation is required in one direction while maintaining insulation in another.

In the Gleeble apparatus, an electric current is conducted through the graphite sheets in a perpendicular direction, thereby generating Joule heating. The heating generated in the specimen is typically much higher than that produced in the sample itself when the specimen exhibits high electrical conductivity, which is the case for aluminum due to its high electrical conductivity. Consequently, the graphite sheet serves not only as a thermal barrier due to its low thermal conductivity, but also contributes to heat generation through the Joule effect, as previously stated by Chugh et al. [27]. Ganapathy et al. [28] demonstrated that the heat transfer coefficients between the specimen and the grips are of critical importance in determining the temperature profile during testing, which is essential for accurate material characterization.

In accordance with Kumar et al. [29], a Gleeble thermomechanical simulator functions by enabling the user to specify a temperature profile over time, denoted by $T_{\mathrm{set}}(t)$. The machine then attains this profile by regulating the current flow through the anvils and the specimen. This capability is essential for accurately replicating the conditions that materials experience during processes such as welding, forging, and hot rolling. Type K thermocouples Tc_1 and Tc_2, with a diameter of $^{10}/_{1000}$ in, are welded directly to the specimen surface at the center of the specimen for the first one and at a distance of 2 mm from the end of the sample for the second one. The temperature is monitored and regulated using the control thermocouple (Tc_1), which provides real-time feedback to a proportional–integral–derivative (PID) control system, while Tc_2 is used to measure the axial thermal gradient within the specimen during the experiment. The system is designed to regulate the current in a manner that ensures the sample adheres to the prescribed temperature profile, thereby facilitating an exact simulation of thermal and mechanical processes. A third Type

K thermocouple, designated as Tc_3, is positioned on the rear surface of the anvil backer. This allows for the acquisition of valuable data regarding the thermal gradient within the anvil itself throughout the course of the experiment. The small diameter of the wires minimizes the impact on the specimen while still providing accurate point temperature measurement. To prevent electrical shorting between the thermocouple wires at locations other than the specimen, the wires were sheathed with PFA (perfluoroalkoxy) tubing and alumina thin tubes near the hot junction.

It is important to note that the design and placement of thermocouples can introduce additional errors. For example, Yang et al. [30] discuss how the welding of thermocouples can result in measurement errors. They suggest that the thermal contact resistance at the junction can distort temperature readings. Zhao et al. [31] demonstrate that the heat dissipation from the thermocouple itself can create a localized temperature drop at the contact point. As reported by Zhang et al. [32], an alternative approach relies on infrared thermography, which offers a non-contact, real-time temperature measurement method that provides uniform temperature profiles across specimen surfaces, thereby overcoming limitations associated with thermocouple-induced thermal gradients and measurement device interference. Infrared pyrometers can also be used, but it is essential to give careful consideration to factors such as emissivity, measurement spot size, and surface conditions.

2.2. Experiments and Results

The chemical composition analysis of Al 2017-T4, conducted using a spark optical emission spectrometer (model Foundry Master Xpert, Oxford Instruments, now Hitachi High-Tech Analytical Science Limited, Abingdon, UK), is presented in Table 1. The results demonstrate a high degree of concordance with the material specifications, with all elements falling within the prescribed ranges.

Table 1. Chemical composition of Al 2017-T4. Al = balance.

Element	Cu	Mg	Mn	Si	Fe	Zn	Cr
Wt %	3.68	0.590	0.554	0.640	0.544	0.144	0.040

To substantiate the proposed approach and the electro-thermal model presented in the subsequent section, we have devised and implemented a comprehensive experimental protocol. A series of three tests was conducted at temperatures of 300, 400, and 500 °C, respectively. For the sake of brevity, only the results obtained at 400 °C will be presented in detail hereafter. The experimental data demonstrate consistent behavioral patterns across various trials, with the primary distinction being the modulation of amplitude magnitudes as the set-point temperature is incrementally elevated in the range from 300 °C to 500 °C. The experimental procedure commenced with an initial temperature of $T_0 = 20$ °C, followed by an initialization phase during which a compressive force of $F = 0.5$ kN was applied linearly over a period of five seconds. Subsequently, the temperature was increased at a rate of 2 °C/s, commencing from $T_{set} = 0$ °C (i.e., no heating is applied until $T_{set} > T_0$). Upon reaching the target temperature of $T_{set} = 400$ °C, the specimen was maintained at this temperature for a duration of 15 min. Subsequently, the heating system was deactivated, and the cooling phase was monitored with continuous data recording for an additional 15 min. The total duration of data acquisition for this test was 2005 s, with measurements recorded at a frequency of 10 Hz, encompassing the entire thermal cycle from initial heating to final cooling.

Figure 3 depicts the temporal evolution of the setpoint (T_{set}), measurements from three thermocouples (Tc_1, Tc_2, and Tc_3), and the heating power value (P).

As illustrated in Figure 3, the temperature readings obtained from thermocouples Tc_1 and Tc_2 closely align with the setpoint temperature T_{set} during the temperature rise and soaking phases at 400 °C. Upon termination of the heating setpoint after 1105 s, thermocouples Tc_1 and Tc_2 demonstrate the sample's natural cooling, with the temperature

decreasing to 26 °C by the conclusion of the test. The temperature of thermocouple Tc_3 reaches a maximum value of 161.5 °C and exhibits variation with a significant delay relative to the setpoint, a consequence of the mass of the anvils and the presence of a cooling system that circulates water regulated at 20 °C. This measurement indicates that models like those proposed by Gao et al. [3] or Zhao et al. [31], which assume a constant temperature of 20 °C at the anvil's rear face, are an inadequate representation of reality, primarily due to the cooling circuit not passing at the anvil's rear face level but approximately 30 mm to 50 mm behind it, at the copper contact plates' level. The significance of this phenomenon on the sample's free cooling curve and the heating power calculation will be revisited in the section dedicated to electro-thermal simulation. The heating power, designated as $P(t)$, is observed to exhibit nonlinear variation with respect to the temperature setpoint, which is represented by the function $T_{\text{set}}(t)$. The observed maximum of 3.16% of the machine's capacity during the heating phase is likely to correspond to the peak power demand when the temperature is rapidly increased. The subsequent decrease to 2.3% during the soaking phase at 400 °C reflects the lower power requirement to compensate for heat losses and maintain a steady temperature.

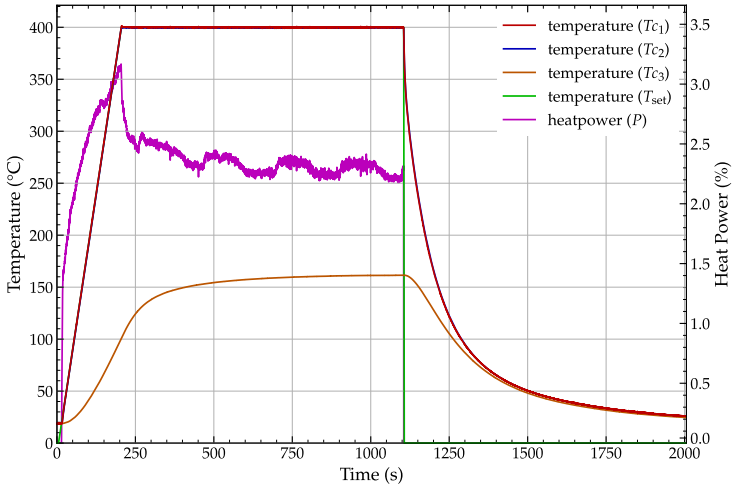

Figure 3. Experimental results extracted from the Gleeble.

As illustrated in Figure 4, which provides a magnified view of the temperature ramp-up period and the 400 °C soaking phase, the Tc_1 temperature closely adheres to the user-defined setpoint temperature T_{set}, with a maximum measured overshoot of 0.36 °C occurring at 205 s of the total time.

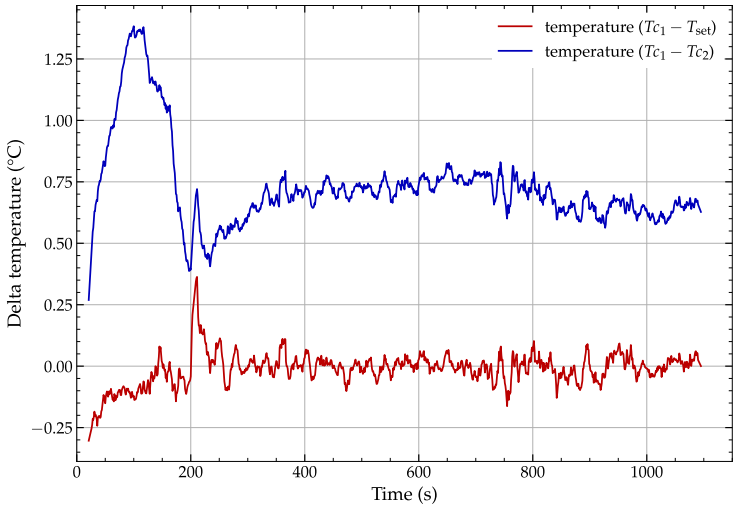

Figure 4. Overshoots extracted from the Gleeble (zoom).

This overshoot coincides with the transition point between the heating phase, which has a rate of 2°C/s, and the constant temperature soaking zone evidenced by the evolution of the $Tc_1 - T_{set}$ curve. Overall, the temperatures measured at points Tc_1 and Tc_2 exhibit a high degree of proximity, as illustrated by the plot $Tc_1 - Tc_2$, with a maximum discrepancy of 0.75 °C observed in the 400 °C soaking zone.

3. Electro-Thermal Simulation of Compression Configuration

The application of electro-thermal modeling and simulation is of paramount importance for the comprehension of the interrelationship between electrical and thermal fields in a multitude of engineering contexts. In their study, Zhang et al. [32] proposed a coupled electro-thermo-mechanical simulation of a Gleeble tensile test, emphasizing the complex interactions that occur during such experiments and the significant thermal gradients in both the axial and radial directions during these tests, leading to the heterogeneous deformation of the specimen. To address these effects, an inverse finite element modeling approach was developed to identify constitutive parameters for ultra-high-strength steel based on Gleeble tests [33].

In their research, Kardoulaki et al. [34] proposed an electro-thermal model to determine temperature gradients during tensile tests using Abaqus/Implicit and a user amplitude (UAMP) subroutine to investigate the impact of these gradients on strain states in materials. The UAMP subroutine calculates the requisite current density to maintain the target temperature, which is analogous to the PID control employed in Gleeble thermo-mechanical simulators. Similarly, in 2015, Ganapathy et al. [35] utilized a UAMP subroutine and Abaqus to investigate the true stress–strain behavior of materials under hot stamping conditions during tensile tests. In 2018, the same first author [28] extended this approach to propose a new grip design. Gao et al. [3] developed an electro-thermal model for the compression behavior of Ti-6Al-4V specimens, incorporating graphite sheets to mitigate friction between anvils and samples while accounting for multi-part anvil construction. Xiao et al. [6] proposed an electro-thermo-mechanical model utilizing Abaqus and a UAMP routine to simulate the compression of near-alpha TA15 titanium, accounting for the sample–anvil interface and providing a comprehensive analysis of the mechanical behavior under compression. These studies demonstrate the significance of advanced modeling techniques in understanding and optimizing the thermal and mechanical behavior of materials under diverse testing conditions.

In this study, we restricted our analysis to electro-thermal modeling, with the aim of determining the temperature fields within the sample and the anvils during the heating and cooling phases of the specimen. The Abaqus/Standard FEM code and a UAMP subroutine have been selected for determining the current density $i(t)$ to be applied based on the desired temperature $T_{set}(t)$, as previously presented. The following subsection is dedicated to the presentation of the proposed UAMP subroutine.

3.1. Definition and Implementation of the UAMP Subroutine

As previously reported by Xiao et al. [6], the initial algorithm proposed by Kardoulaki et al. [34] for controlling thermal behavior, when applied to our study case, exhibited poor performance, leading to thermal oscillations. The implementation of the model proposed by [6] also presented certain difficulties, largely due to the lack of sufficient details concerning its actual implementation within the Abaqus code. Therefore, we proceeded to develop a novel algorithm for determining the current density, $i(t)$, from the setpoint temperature, $T_{set}(t)$, as detailed in the following sections.

At time t, that is, at increment k of an implicit time integration scheme, if the setpoint temperature $T_{set}(k)$ exceeds the ambient temperature T_0, a PID controller is employed to calculate the new current density $i(k)$ to be applied to the external surfaces of the anvils. The temperature error, denoted by $\Delta T_p(k)$, is then defined as follows:

$$\Delta T_p(k) = T_{set}(k) - Tc_1(k), \quad (1)$$

where $Tc_1(k)$ represents the temperature measured at time step k by the thermocouple sensor node positioned at the center of the specimen's surface. A discrete PID control is implemented using this error to calculate the corrective thermal term, denoted as $\Delta T_h(k)$, for the increment k:

$$\Delta T_h(k) = K_p \cdot \Delta T_p(k) + K_i \sum_{i=0}^{k} \left[\Delta t \cdot \Delta T_p(i)\right] + K_d \frac{\Delta T_p(k) - \Delta T_p(k-1)}{\Delta t}, \tag{2}$$

where K_p is the proportional gain, K_i is the integral gain, and K_d is the derivative gain of the PID controller. The current time increment, defined by the implicit integration scheme used, is denoted as Δt.

In consideration of the configuration of the anvils, as illustrated in Figure 5, let S_1 be defined as the cross-sectional area of the sample where the thermocouple Tc_1 is welded (right surface), and let S_2 be defined as the surface area where the current $i(t)$ is applied (left surface). In Figure 5, GF represents a stack of graphite foils.

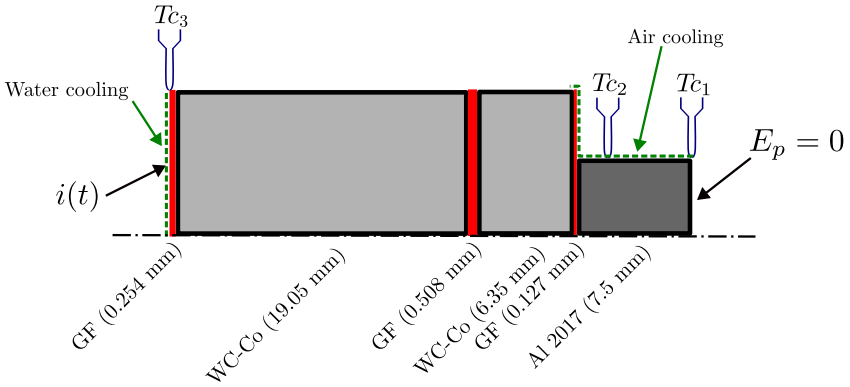

Figure 5. Electro-thermal axi-symmetric model used for the numerical simulations. Where $i(t)$: applied current density, Tc_1: monitored and regulated temperatures using control thermocouple, Tc_2: the axial thermal gradient within the specimen during the experiment, Tc_3: K thermocouple, positioned on the rear surface of the anvil backer.

If only one material is taken into account and if all surfaces can be considered adiabatic, then according to Joule's law and Equation (2), the new current density, $i(k)$, can be computed as follows:

$$i(k) = \frac{S_1}{S_2}\sqrt{\frac{\rho\sigma C_p \Delta T_h(k)}{\Delta t}} = \gamma\sqrt{\frac{\Delta T_h(k)}{\Delta t}}, \qquad \text{with} \qquad \gamma = \frac{S_1}{S_2}\sqrt{\rho\sigma C_p}, \tag{3}$$

where ρ is the material density, C_p is the specific heat capacity, and σ is the electrical conductivity. In a coupled electro-thermal model, the aforementioned quantities can be either constant or dependent on the current temperature. When considering an assembly of materials with disparate electro-thermal properties, the value of the γ coefficient in Equation (3) can be replaced in the following form:

$$\gamma = \frac{S_1}{S_2}\sqrt{\frac{\sum_i V_i}{\sum_i \frac{V_i}{\rho_i \sigma_i C_{p_i}}}}, \tag{4}$$

where $\square_i$ defines a quantity relative to material i of the considered assembly and V_i is the volume of the considered material. When only a single material is considered, Equation (4) simplifies to the form of Equation (3), i.e., $\gamma = \frac{S_1}{S_2}\sqrt{\rho\sigma C_p}$. The evaluation of the γ coefficient from Equation (4) is approximate and does not take into account the exact geometry of the material assemblies or the interface conditions between these materials can serve as an initial value for a search for optimal convergence parameters of the PID.

With regard to the implementation of the UAMP, two internal state variables (SVARS) are utilized in Abaqus for the storage of terms pertaining to temperature increments for the temperature control algorithm. The first variable stores the cumulative term $\sum_{i=0}^{k}\left[\Delta t \cdot \Delta T_p(i)\right]$ for computing the integral term, while the second stores the previous temperature increment $\Delta T_p(k)$ for the derivative term, ensuring continuity and accuracy across increments. The algorithm is implemented using the Fortran 77 programming language, and the UAMP subroutine, which was developed for use with Abaqus 2024 [13], includes initialization, a user-defined setpoint temperature $T_{\text{set}}(t)$, and comprehensive data tracking options, enhancing the usability and effectiveness of the subroutine.

3.2. Numerical Models

Figure 5 depicts a schematic representation of the electro-thermal model utilized in our simulation, delineating the fundamental hypotheses underlying the simulation. The dimensions of the anvils and sample are provided in the experimental setup in Section 2.1. The axi-symmetric half numerical model implemented in Abaqus comprises three materials: the 2017-T4 aluminum specimen; the ISO-T anvils, which consist of two WC-Co parts with a diameter of 3/4 in, and respective lengths of 1/4 in for the cap and 3/4 in for the backer; and the various graphite foils that constitute the interfaces between the different materials. The stacking sequence of materials and the different longitudinal dimensions are reported in Figure 5.

The thermal and electrical properties of the 2017-T4 aluminum alloy, graphite sheets, and WC-Co anvils were primarily sourced from the existing literature and material data sheets. The thermophysical properties of the 2017-T4 aluminum alloy have been the subject of some research, but it may not be considered as extensively studied as other, more common aluminum alloys, such as the 2024-T4 alloy. The basic thermal properties of the material, including electrical conductivity (σ), thermal conductivity (λ), specific heat (C_p), and density (ρ), are available in the ASM International Handbooks [36,37]. However, the dependence of these properties on temperature is not included. With regard to the WC-Co anvils, the thermo-physical properties were derived from Xiao et al. [6]. Table 2 presents a synthesis of the principal thermo-electrical properties at $T = 20$ °C of diverse materials.

Table 2. Material parameters used in the numerical simulations at $T = 20$ °C.

	ρ (g/cm^3)	λ (W/m°C)	C_p (J/kg°C)	σ (S/mm)
2017-T4 [36]	2.796	134.13	880	19,720
Tungsten [6]	14.430	70.52	220	2000
Graphite [20]	1.135	5.39	711	1.5

In consideration of the dimensions of the various components in the model and the material properties of the three materials outlined in Table 2, the value of γ provided by Equation (4) is $\gamma = 0.094$ for our model. The coefficients utilized for the numerical simulations of the PID controller are $K_p = 2.2$ and $K_i = K_d = 1.1$.

An electric potential of $E_p = 0$ is imposed on the right surface of the model, serving as the reference potential. The current density, $i(t)$, computed using the UAMP subroutine in accordance with Equation (3), is imposed on the left surface, thereby driving the electrical behavior of the system. The initial temperature of the system is set to $T_0 = 20$ °C.

Notwithstanding the fact that the tests were conducted under low-pressure conditions ($P = 40$ Pa), air cooling was taken into account at the level of the sample and the portion of the anvil situated outside the sleeve (zone to the right of Figure 5) had a reference sink temperature of $T_0 = 20$ °C and a reference film coefficient of h = 1 W/m^2 °C. The cooling of the jaws by water circulation is accounted for on the left surface, resulting in a surface film condition (left zone in Figure 5) with a reference sink temperature of $T = 20$ °C and a reference film coefficient of h = 1 W/m^2 °C.

The numerical model is meshed using 4-node bilinear axisymmetric coupled temperature-displacement quadrilateral elements (DCAX4E), with a global size of 0.2 mm for each element. This results in a total of 7286 elements for the entire model. The aforementioned elements possess both temperature and electric potential degrees of freedom at each node, thereby enabling the modeling of the fully coupled thermal–electrical behavior. The total simulation time is defined by the experimental conditions, with a value of $t = 2005$ s. The time increment of the implicit integration scheme is held constant at $\Delta t = 1$ s.

The numerical simulations were conducted on a Dell XPS-13 7390 laptop, equipped with an Intel 4-core i7-10510U processor and 16 GB of RAM, running the Ubuntu 22.04 LTS 64-bit operating system. The simulations were conducted using the Abaqus/Standard 2024 software [13], with parallel processing enabled on three cores to optimize computational efficiency. The total computing time for the two models presented in the following subsection is approximately 6 min and 30 s.

Figure 6 illustrates the Fortran 77 source code for the UAMP subroutine, which calculates the current density $i(t)$ to be applied to the system based on the measured temperature at control point Tc_1.

```
C F77 UAMP subroutine to compute i(t) as function of TC1 and Tset
      Subroutine UAMP(ampName, time, ampValueOld, dt, nProps, props, nSvars, svars,
     + lFlagsInfo, nSensor, sensorValues, sensorNames, jSensorLookUpTable, ampValueNew,
     + lFlagsDefine, AmpDerivative, AmpSecDerivative, AmpIncIntegral, AmpDoubleIntegral)
      include "aba_param.inc"
      dimension jSensorLookUpTable(*)
      dimension sensorValues(nSensor)
      dimension svars(nSvars)
      dimension props(nProps)
      character*80 sensorNames(nSensor)
      character*80 ampName
      dimension time(2)
      dimension lFlagsInfo(4)
      dimension lFlagsDefine(7)
      parameter ( Tref = 20 )
      parameter ( npoints = 7 )
      real timeData(npoints), tempData(npoints)
      data timeData /    0,    5,    5,  205, 1105, 1105, 2005/
      data tempData /   -1,   -1,    0,  400,  400,   -1,   -1/
      lFlagsDefine = 0
      if (ampName(1:7) .eq. 'CURRENT' ) then
        TC1 = GetSensorValue('TC1', jSensorLookUpTable, sensorValues)
C Test if this is the first increment / Initialize the variables
        if (lFlagsInfo(1) .eq. 1) then
          ampValueNew = 0
          svars = 0
        end if
C If it is not the first increment / The ampValueNew has to be computed
        if (lFlagsInfo(2) .eq. 1) then
          ctime = time(1)
          do I=1, npoints-1
            if (ctime .ge. timeData(I) .and. ctime .le. timeData(I+1)) then
              if (tempData(I) .eq. -1) then
                reqTemp = -1
              else
              reqTemp = tempData(I) + (ctime - timeData(I)) *
     +         (tempData(I+1) - tempData(I)) / (timeData(I+1) - timeData(I))
              end if
              exit
            end if
          end do
          if (reqTemp .gt. Tref) then
            tempErr = reqTemp - TC1
            xprop = 2.2 * tempErr
            svars(1) = svars(1) + tempErr * dt
            xint = 1.1 * svars(1)
            xder = 1.1 * (tempErr - svars(2)) / dt
            svars(2) = tempErr
          ampValueNew = 0.094 * sqrt((xprop + xint + xder) / dt)
          end if
          if (reqTemp .eq. -1) then
            ampValueNew = 0
            svars = 0
          end if
        end if
      end if
      return
      end
```

Figure 6. The UAMP F77 subroutine used to compute the current density $i(t)$ for 400 °C.

This subroutine facilitates the specification of the desired temperature, denoted as T_{set}, through the utilization of the `timeData` and `tempData` tables analogous to the command interface observed in the Gleeble thermomechanical simulator. In the context of the subroutine's operational parameters, a temperature value of -1 is indicative of the absence of heating. The various periods are explicitly indicated: no heating between 0 s to 5 s, followed by a ramp of 2 °C s^{-1} from 5 s to 205 s, a hold at 400 °C between the time intervals of 205 s to 1105 s (approximately 15 min), and followed by a free cooling phase from 1105 s to 2005 s (approximately 15 min).

4. Results and Discussion

4.1. Numerical Simulation with Constant Cooling Condition

A preliminary numerical model is proposed, wherein the cooling condition is represented by an imposed temperature of $T = 20$ °C on the left surface. The numerical simulations demonstrated the absence of a temperature gradient within the cylindrical specimen during the Gleeble heating test. Figure 7 illustrates the temperature field within the anvils and the sample at $t = 1100$ s, which corresponds to five seconds prior to the shutdown of the heating system and the commencement of the sample cooling phase.

Figure 7. Temperature contourplot in the anvil and the sample at the end of the heating phase ($t = 1100$ s) for the constant cooling condition.

As illustrated, the temperature within the anvils varies from 401.4 °C to 182.5 °C as the distance from the sample contact zone increases. Conversely, the temperature throughout the entire sample remains constant at approximately 400 °C. Figure 8 (left) provides a close-up view of the sample, the graphite sheet between the sample and the anvil, as well as a portion of the anvil with a thickness of 3 mm. Figure 8 (right) shows only the 2017-T4 aluminum specimen.

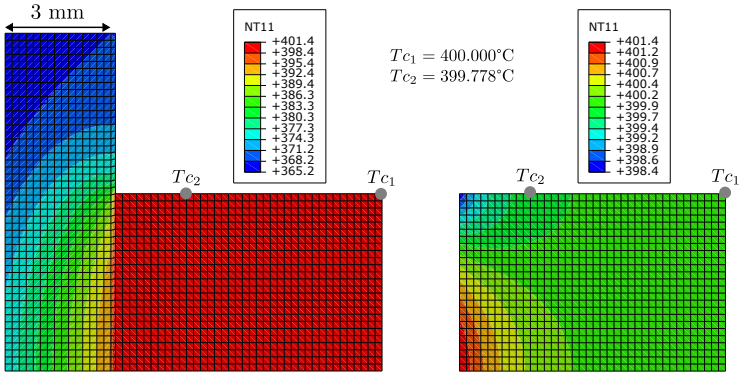

Figure 8. Temperature contourplot in the sample and a portion of the anvil at the end of the heating phase ($t = 1100$ s) for the constant cooling condition.

The temperature scales have been modified to encompass the specified temperature ranges. As observed previously, the temperature of the entire sample falls between 398.4 °C and 401.4 °C, with the two points $Tc_1 = 400$ °C and $Tc_2 = 399.78$ °C exhibiting a high degree of proximity. The maximum temperature is observed at the center of the face in contact with the graphite sheet, while the minimum temperature is located at the edge of the specimen's face. The maximum temperature differential ΔT across the entire specimen is approximately 3 °C. Additionally, the figure illustrates the temperature gradient within the graphite sheet, which reaches a difference of 4 °C between the two faces.

Figure 9 depicts the temporal evolution of temperature Tc_1, calculated by Abaqus, and the experimentally measured temperature Tc_1^{exp}.

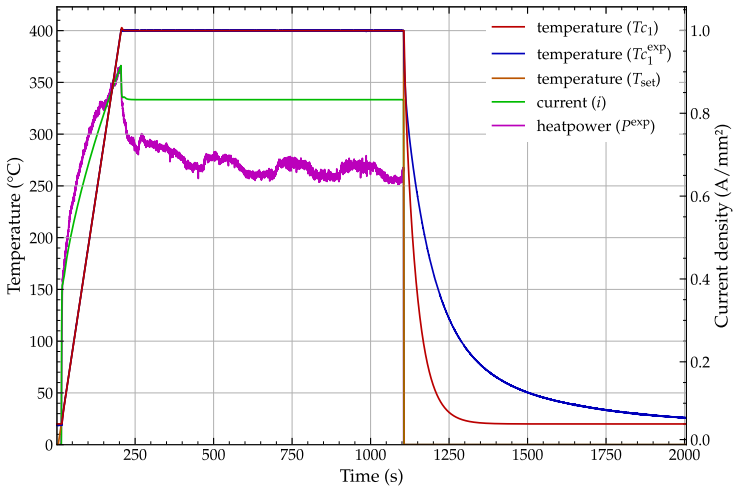

Figure 9. Temporal evolution of the numerically calculated and experimentally measured temperatures Tc_1, the current density i, and the heating power P^{exp} for the constant cooling condition.

A strong correlation between these two results is evident throughout the entire heating phase and the holding period at 400 °C. The free cooling curves differ between the numerical results, designated as Tc_1, and the experimental results, designated as Tc_1^{exp}. This discrepancy is notable due to the poor representation of the cooling process by an imposed surface temperature of $T = 20$ °C. While there are differences between theoretical and experimental cooling curves, they may not be significant when the tests are considered in their original context, as the key is to accurately predict the temperature gradient during compression. Since air or water quenching is generally used to preserve the microstructure, which drastically changes the cooling kinetics, numerical simulations of the cooling phase are not strictly necessary. The experimental and numerical measurements of Tc_1 demonstrate a close alignment with the imposed temperature evolution, as defined by T_{set}. The numerical cooling rate is considerably higher than the experimental cooling rate. This discrepancy can be rectified by adjusting the reference film coefficient h used in the definition of the surface film condition, as proposed by several authors. The adjustment process involves identifying the coefficient by minimizing the difference between experimental and computed values. In the current study, this approach has led to a value of approximately $h = 750$ W/m^{2}K.

Additionally, the figure illustrates the evolution of the current density i applied to the device and the experimental heating power P^{exp}. As these two quantities do not correspond to identical terms and do not represent exactly the same quantity, $i_{max} = 0.915$ A/mm^2 and $P^{exp}_{max} = 3.14\%$. As illustrated in Figure 3, the P^{exp} curve has been rescaled on the ordinate axis to facilitate comparison between the curves. Therefore, a favorable correlation is evident between the current density, as defined by the UAMP subroutine, and the experimental heating power, as observed in the Gleeble during the temperature ramp-up phase during the temperature holding phase. The subsequent subsections will address this discrepancy.

4.2. Numerical Simulation with Variable Cooling Condition

In the Gleeble thermomechanical simulator, the jaws are cooled by circulating water at a temperature of $T = 20$ °C inside the machine jaws, specifically at a certain distance from the rear surface of the anvil. This is demonstrated by the variation in the evolution of the Tc_3 temperature (which reaches $Tc_3 = 161.5$ °C) in Section 2.2. To enhance the precision of the numerical results pertaining to the cooling kinetics of the sample, a second numerical model is proposed. In this model, the sink temperature applied to the rear face of the anvils is no longer a constant value of $T = 20$ °C throughout the simulation. Instead, it is set to the temperature Tc_3, which was recorded during the experimental tests. As illustrated in Figure 10, the modification of the thermal boundary condition has a negligible impact on

the results. The figure presents a close-up view of the sample and the temperature field at $t = 1100$ s.

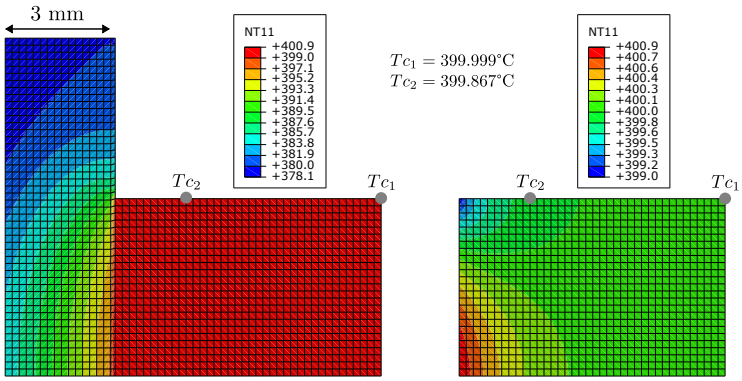

Figure 10. Temperature contourplot in the sample and a portion of the anvil at the end of the heating phase ($t = 1100$ s) for the variable cooling condition.

The total temperature differential within the sample reaches $\Delta T = 1.9$ °C, with a maximum temperature of $T = 400.9$ °C at the center of the sample face and a minimum temperature of $T = 399.0$ °C at the edge of the sample face, as previously observed. The two temperatures, designated as Tc_1 and Tc_2, remain in close proximity to one another, with a difference of only $\Delta T = 0.13$ °C ($Tc_1 = 400.00$ °C and $Tc_2 = 399.87$ °C).

Figure 11 illustrates the temporal evolution of the numerically calculated and experimentally measured temperatures, designated as Tc_1, in addition to the evolution of the current density, represented by i. This figure presents a similar representation to that observed in Figure 9.

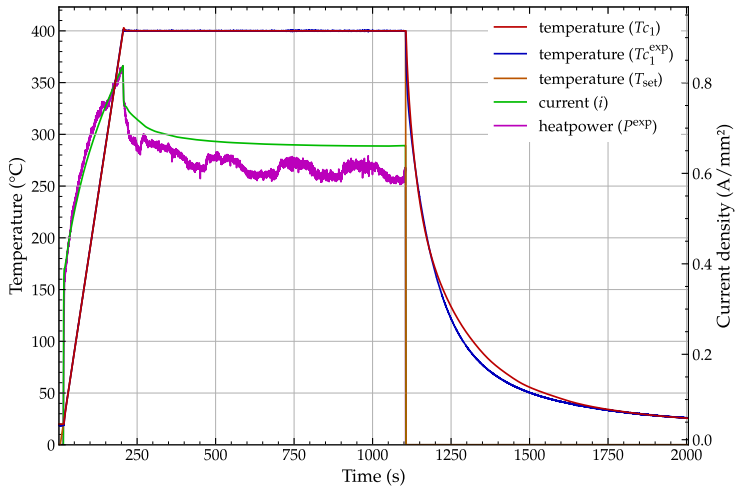

Figure 11. Temporal evolution of the numerically calculated and experimentally measured temperatures Tc_1, the current density i, and the heating power P^{exp} for the variable cooling condition.

With regard to the thermal outcomes, the heating phase and the holding period at 400 °C are, in general, identical to those reported in Section 4.1. With regard to the free cooling of the sample subsequent to the heating phase, a pronounced correlation is evident between the numerical and experimental results for the temporal evolution of Tc_1 and Tc_1^{exp}. The maximum current density in this model is $i_{max} = 0.84$ A/mm^2, which is lower than that of the constant cooling case. This is in accordance with the physics of the process. After the temperature rise phase, the current density ($i(t)$) exhibits an evolution that is much more consistent with the evolution of the heat power (P^{exp}) compared to the previous case.

5. Conclusions

This study presents an experimental and numerical investigation of the temperature fields that develop in 2017-T4 aluminum alloy specimens prior to Gleeble compression tests at elevated temperatures up to 500 °C. The principal findings and conclusions of the present study are as follows:

- The experimental temperature measurements, which were conducted using multiple thermocouples that were welded to the specimen and anvils, revealed that there were minimal temperature differences between the center and 2 mm from the end of the specimen during the heating process, with the temperature rising to 400 °C. These temperature differences were found to be less than 1 °C.
- A coupled thermal–electrical finite element model developed in Abaqus with a user subroutine (UAMP) to control the heating exhibited a high degree of correlation with the experimental temperature measurements. The simulations indicate that minimal temperature gradients (<1.9 °C) will be observed within the specimen at the conclusion of the heating process, reaching 400 °C. This is attributed to the specific configuration of graphite foils within the anvil assemblies and on the anvil faces.
- The graphite foils, which are positioned between the specimen and the anvils, as well as between the anvil components, serve to mitigate the temperature gradients within the specimen by functioning as thermal and electrical insulators.
- The use of the measured anvil temperature as a boundary condition in lieu of a constant temperature of 20 °C resulted in a notable enhancement in the alignment between the simulated and experimental cooling curves following the heating phase.
- The UAMP subroutine has been developed to effectively mimic the Gleeble's PID temperature control system, calculating the requisite current density to follow the specified temperature profile. The numerically predicted heating power exhibits a high degree of correlation with the experimental measurements.

The thermal gradient observed for the 2017-T4 aluminum alloy under the conditions studied here is relatively modest. However, temperature gradients at the end of the heating phase in Gleeble compression specimens have the potential to introduce uncertainties in the measured flow stress and mechanical properties. It is therefore essential to have accurate numerical models that are capable of capturing these gradients in order to interpret and correct Gleeble test results in order to obtain the true material behavior. The experimental–numerical approach presented here, and in particular the UAMP subroutine, provides a framework for quantifying the initial temperature gradients in Gleeble compression specimens and for assessing their impact on the measured constitutive response of materials at elevated temperatures.

Ongoing exploratory work includes extending these studies to other materials such as nickel-based superalloys, where the study temperatures exceed 1000 °C. The conditions are altered not only by the elevated temperatures, but also by the fact that these alloys are significantly less electrically conductive than aluminum. This will have a significant effect on the current flowing through the anvils and graphite plates. Regarding the proposed approach to numerical modeling, the change in material and temperature range requires a phase of identification of thermoelectric parameters and adjustments to the boundary conditions of the model. Nevertheless, as in the present case, some experimental tests should allow for the calibration of the model and the validation of its predictive capabilities.

Author Contributions: Conceptualization, O.P.; methodology, O.P.; software, O.P.; validation, O.P.; formal analysis, O.P.; investigation, Y.M.; resources, O.P. and Y.B.; data curation, O.P. and Y.M.; writing—original draft preparation, O.P.; writing—review and editing, O.P. and Y.B.; visualization, O.P.; supervision, O.P. and Y.B.; project administration, O.P. and Y.B.; funding acquisition, O.P. and Y.B. All authors have read and agreed to the published version of the manuscript.

Funding: This research received no external funding.

Institutional Review Board Statement: Not applicable.

Informed Consent Statement: Not applicable.

Data Availability Statement: The data presented in this study are openly available in Zenodo at at DOI 10.5281/zenodo.13859634, reference number 13859635.

Conflicts of Interest: The authors declare no conflicts of interest.

Abbreviations

The following abbreviations are used in this manuscript:

UAMP	User amplitude subroutine
PID	Proportional–integral–derivative
FE	Finite element
FEM	Finite element method
DIC	Digital image correlation
DRX	Dynamic recrystallization
PFA	Perfluoroalkoxy
WC-Co	Tungsten carbide–cobalt
ISO-T	Designation for specific tungsten carbide anvils used in Gleeble tests

References

1. Zhang, R.; Shao, Z.; Lin, J.; Dean, T.A. Measurement and Analysis of Heterogeneous Strain Fields in Uniaxial Tensile Tests for Boron Steel Under Hot Stamping Conditions. *Exp. Mech.* **2020**, *60*, 1289–1300. [CrossRef]
2. Bennett, C.; Leen, S.; Williams, E.; Shipway, P.; Hyde, T. A critical analysis of plastic flow behaviour in axisymmetric isothermal and Gleeble compression testing. *Comput. Mater. Sci.* **2010**, *50*, 125–137. [CrossRef]
3. Gao, T.; Ma, L.; Peng, X.G. Study on Temperature Distribution of Specimens Tested on the Gleeble 3800 at Hot Forming Conditions. *J. Electron. Sci. Technol.* **2014**, *12*, 5. [CrossRef]
4. Quan, G.Z.; Pan, J.; Zhang, Z.h. Phase transformation and recrystallization kinetics in space–time domain during isothermal compressions for Ti–6Al–4V analyzed by multi-field and multi-scale coupling FEM. *Mater. Des.* **2016**, *94*, 523–535. [CrossRef]
5. Jedrasiak, P.; Shercliff, H.; Mishra, S.; Daniel, C.S.; Da Fonseca, J.Q. Finite Element Modeling of Hot Compression Testing of Titanium Alloys. *J. Mater. Eng. Perform.* **2022**, *31*, 7160–7175. [CrossRef]
6. Xiao, H.; Fan, X.; Zhan, M.; Liu, B.; Zhang, Z. Flow stress correction for hot compression of titanium alloys considering temperature gradient induced heterogeneous deformation. *J. Mater. Process. Technol.* **2021**, *288*, 116868. [CrossRef]
7. Huang, K.; Logé, R. Microstructure and flow stress evolution during hot deformation of 304L austenitic stainless steel in variable thermomechanical conditions. *Mater. Sci. Eng.* **2018**, *711*, 600–610. [CrossRef]
8. Zhang, J.; Yi, Y.; Huang, S.; Mao, X.; He, H.; Tang, J.; Guo, W.; Dong, F. Dynamic recrystallization mechanisms of 2195 aluminum alloy during medium/high temperature compression deformation. *Mater. Sci. Eng.* **2021**, *804*, 140650. [CrossRef]
9. Yu, D.; Xu, D.; Wang, H.; Zhao, Z.; Wei, G.; Yang, R. Refining constitutive relation by integration of finite element simulations and Gleeble experiments. *J. Mater. Sci. Technol.* **2019**, *35*, 1039–1043. [CrossRef]
10. Coelho, B.; Thuillier, S. On the use of the Gleeble® test as a heterogeneous test: Sensitivity analysis on temperature, strain and strain rate. *IOP Conf. Ser. Mater. Sci. Eng.* **2022**, *1238*, 012058. [CrossRef]
11. Cheng, M.; Wu, X.; Zhang, Z. Study of the Dynamic Recrystallization Behavior of Mg-Gd-Y-Zn-Zr Alloy Based on Experiments and Cellular Automaton Simulation. *Metals* **2024**, *14*, 570. [CrossRef]
12. Tize Mha, P.; Dhondapure, P.; Jahazi, M.; Tongne, A.; Pantalé, O. Artificial Neural Network-Based Critical Conditions for the Dynamic Recrystallization of Medium Carbon Steel and Application. *Metals* **2023**, *13*, 1746. [CrossRef]
13. Dassault Systèmes. *Abaqus Reference Manual*; Vélizy-Villacoublay: Paris, France, 2024.
14. Bennett, C.J.; Leen, S.B.; Shipway, P.H. A Finite Element Analysis of Errors in Axisymmetricisothermal and Gleeble Compression Testing of Ti-6Al-4V. *Int. J. Mater. Form.* **2010**, *3*, 1155–1158. [CrossRef]
15. Bennett, C.J.; Sun, W. Optimisation of material properties for the modelling of large deformation manufacturing processes using a finite element model of the Gleeble compression test. *J. Strain Anal. Eng. Des.* **2014**, *49*, 429–436. [CrossRef]
16. Åkerström, P.; Wikman, B.; Oldenburg, M. Material parameter estimation for boron steel from simultaneous cooling and compression experiments. *Model. Simul. Mater. Sci. Eng.* **2005**, *13*, 1291–1308. [CrossRef]
17. Wei, X.H.; Liu, L.; Zhang, J.X.; Shi, J.L.; Guo, Q.G. Mechanical, electrical, thermal performances and structure characteristics of flexible graphite sheets. *J. Mater. Sci.* **2010**, *45*, 2449–2455. [CrossRef]
18. Pollock, M. *Grafoil-Engineering Design Manual*; Technical Report; Graftech Inc.: Brooklyn Heights, OH, USA, 2002.
19. Fu, Y.; Hou, M.; Liang, D.; Yan, X.; Fu, Y.; Shao, Z.; Hou, Z.; Ming, P.; Yi, B. The electrical resistance of flexible graphite as flowfield plate in proton exchange membrane fuel cells. *Carbon* **2008**, *46*, 19–23. [CrossRef]
20. Cermak, M.; Perez, N.; Collins, M.; Bahrami, M. Material properties and structure of natural graphite sheet. *Sci. Rep.* **2020**, *10*, 18672. [CrossRef]

21. Chen, P.H.; Chung, D. Thermal and electrical conduction in the compaction direction of exfoliated graphite and their relation to the structure. *Carbon* **2014**, *77*, 538–550. [CrossRef]
22. Solfiti, E.; Berto, F. A review on thermophysical properties of flexible graphite. *Procedia Struct. Integr.* **2020**, *26*, 187–198. [CrossRef]
23. Inagaki, M.; Kaburagi, Y.; Hishiyama, Y. Thermal Management Material: Graphite. *Adv. Eng. Mater.* **2014**, *16*, 494–506. [CrossRef]
24. Janerka, K.; Jezierski, J.; Stawarz, M.; Szajnar, J. Method for Resistivity Measurement of Grainy Carbon and Graphite Materials. *Materials* **2019**, *12*, 648. [CrossRef] [PubMed]
25. Sariyev, B.; Abdikadyr, A.; Baitikenov, T.; Anuarbekov, Y.; Golman, B.; Spitas, C. Thermal properties and mechanical behavior of hot pressed PEEK/graphite thin film laminate composites. *Sci. Rep.* **2023**, *13*, 12785. [CrossRef] [PubMed]
26. Gong, F.; Li, H.; Wang, W.; Xia, D.; Liu, Q.; Papavassiliou, D.; Xu, Z. Recent Advances in Graphene-Based Free-Standing Films for Thermal Management: Synthesis, Properties, and Applications. *Coatings* **2018**, *8*, 63. [CrossRef]
27. Chugh, R.; Chung, D. Flexible graphite as a heating element. *Carbon* **2002**, *40*, 2285–2289. [CrossRef]
28. Ganapathy, M.; Li, N.; Lin, J.; Abspoel, M.; Bhattacharjee, D. A Novel Grip Design for High-Accuracy Thermo-Mechanical Tensile Testing of Boron Steel under Hot Stamping Conditions. *Exp. Mech.* **2018**, *58*, 243–258. [CrossRef]
29. Kumar, V. Thermo-mechanical simulation using gleeble system-advantages and limitations. *J. Metall. Mater. Sci.* **2016**, *58*, 81–88.
30. Yang, R.; Yu, D.; Xu, D. Influence of thermocouple welding on the Gleeble temperature measurement error and a scheme for its correction. *Sci. Sin. Technol.* **2021**, *51*, 185–194. [CrossRef]
31. Zhao, X.; Ma, Y.; Gao, S.; Li, X.; Yu, D.; Wang, H. Nonnegligible Temperature Drop Induced by Thermocouple on Samples in Gleeble Tests. *Metals* **2023**, *13*, 1573. [CrossRef]
32. Zhang, C.; Bellet, M.; Bobadilla, M.; Shen, H.; Liu, B. A Coupled Electrical–Thermal–Mechanical Modeling of Gleeble Tensile Tests for Ultra-High-Strength (UHS) Steel at a High Temperature. *Metall. Mater. Trans. A* **2010**, *41*, 2304–2317. [CrossRef]
33. Zhang, C.; Bellet, M.; Bobadilla, M.; Shen, H.; Liu, B. Inverse finite element modelling and identification of constitutive parameters of UHS steel based on Gleeble tensile tests at high temperature. *Inverse Probl. Sci. Eng.* **2011**, *19*, 485–508. [CrossRef]
34. Kardoulaki, E.; Lin, J.; Balint, D.; Farrugia, D. Investigation of the effects of thermal gradients present in Gleeble high-temperature tensile tests on the strain state for free cutting steel. *J. Strain Anal. Eng. Des.* **2014**, *49*, 521–532. [CrossRef]
35. Ganapathy, M.; Li, N.; Lin, J.; Abspoel, M.; Guido, H.; Bhattacharjee, D. Analysis of new Gleeble tensile specimen design for hot stamping application. *MATEC Web Conf.* **2015**, *21*, 05013. [CrossRef]
36. Davis, J.R. *Aluminum and Aluminum Alloys*, 6th ed.; ASM specialty handbook; ASM International: Materials Park, OH, USA, 2007.
37. ASM International. *ASM Handbook: Nonferrous Alloys and Special-Purpose Materials*, 10th ed.; Metals handbook; ASM International: Materials Park, OH, USA, 1992.